Cellulose (2021) 28:1369–1385
https://doi.org/10.1007/s10570-020-03590-z

ORIGINAL RESEARCH

Characterization of the supramolecular structures of cellulose nanocrystals of different origins

Umesh P. Agarwal · Richard S. Reiner · Sally A. Ralph · Jeffery Catchmark · Kai Chi · E. Johan Foster · Christopher G. Hunt · Carlos Baez · Rebecca E. Ibach · Kolby C. Hirth

Received: 18 June 2020 / Revised: 9 November 2020 / Accepted: 12 November 2020 / Published online: 6 January 2021

Abstract Properties of cellulose nanocrystals (CNCs) depend upon their supramolecular structures, which are important to understand in order to optimize their applications. In this investigation, the structures of CNCs produced upon 48–64% H_2SO_4 hydrolysis of hydrothermally-treated poplar, bleached kraft pulp, cotton microcrystalline cellulose, bacterial cellulose, tunicin, and cladophora cellulose were comparatively analyzed. TEM provided information on the morphological aspects. Raman, MAS-NMR, and XRD provided information on one aspect of the supramolecular organization, namely, crystallinity (CrI). Other characteristics of supramolecular structure were analyzed by various Raman methods, namely, accessibility to water, exocyclic CH_2OH conformation ratio, and chain conformation disorder (CCONDIS)—the last method was developed in the present study. In general, CNCs retained the crystallinity of the starting material irrespective of the measurement method of CrI. Additionally, it was found that crystallite size and supramolecular organization influenced CrI as well. These analyses further indicated that poplar- and pulp-CNCs had significantly higher water accessibility as compared with CNCs from cladophora, bacterial, tunicin, and cotton MCC CNCs, implying higher molecular disorder, which was also reflected in measurements of CH_2OH conformation ratio and CCONDIS. The findings indicate that significant differences among the CNCs seem to arise largely from differences between the starting materials. Additionally, considering that CNCs can have very different morphologies and structural properties depending upon how they are produced, the analyses carried out here can characterize such CNCs and estimate their applications.

Electronic supplementary material The online version of this article (https://doi.org/10.1007/s10570-020-03590-z) contains supplementary material, which is available to authorized users.

U. P. Agarwal (✉) · R. S. Reiner · S. A. Ralph · C. Baez
Fiber and Chemical Sciences Research, USDA FS, Forest Products Laboratory, 1 Gifford Pinchot Drive, Madison, WI 53726-2398, USA
e-mail: umesh.p.agarwal@usda.gov

J. Catchmark · K. Chi
Agricultural and Biological Engineering, Pennsylvania State University, University Park, PA 16802, USA

E. J. Foster
Department of Chemical and Biological Engineering, University of British Columbia, Vancouver, BC V6T 1Z3, Canada

C. G. Hunt · R. E. Ibach
Forest Biopolymer Science and Engineering, USDA FS, Forest Products Laboratory, 1 Gifford Pinchot Drive, Madison, WI 53726-2398, USA

K. C. Hirth
Analytical Chemistry and Microscopy Laboratory, USDA FS, Forest Products Laboratory, 1 Gifford Pinchot Drive, Madison, WI 53726-2398, USA

Graphic abstract

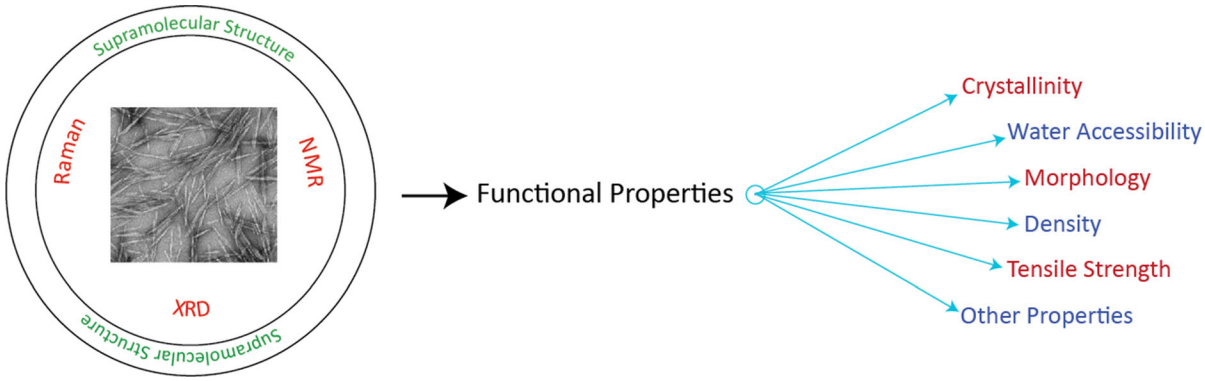

Keywords Cellulose · Tunicin · Bacterial · Cladophora · Wood · Pulp · Cotton · Crystallinity · Raman spectroscopy

Introduction

Cellulose nanocrystals (CNCs) have received much recent attention due to their unique characteristics, such as biodegradability, small size, high crystallinity, birefringence, strong mechanical properties, high charge density and surface to be modified by functionalization (Habibi et al. 2010; Klemm et al. 2011; Moon et al. 2011; Sabo et al. 2016) and amenability to further modification by surface functionalization (Habibi 2014).

CNCs are presently produced commercially by a number of manufacturers (Mao et al. 2017; Mokhena and John 2020) and potential applications are in the fields of regenerative medicine (Domingues et al. 2014; Frost and Foster 2019), optics (Zhang et al. 2012; Kose et al. 2019), composite films (Yu et al. 2013; Natterodt et al. 2017; Smyth et al. 2018), hydrogels (Yang et al. 2013), coatings (Poaty et al. 2014), pharmaceuticals and food packaging (Aulin et al. 2009; Goetz et al. 2009) and automotive sector (Dahlke et al. 1998). They have been prepared from a wide variety of cellulose sources such as tunicin (Angle's and Dufresne 2000), algae (Horikawa et al. 2018), cotton (Heux et al. 2000), bacterial cellulose (Grunert and Winter 2002), sugar beet (Azizi et al. 2004), wood (Agarwal et al. 2018a, Abushammala et al. 2015), wood-pulp (Bian et al. 2017; Chen et al. 2015, 2016; Bondeson et al. 2006; Kvien et al. 2005), ramie (Lu et al. 2006), and rice & wheat straws (Jiang and Hsich 2017, Helbert et al. 1996). The predominant material of choice has been bleached kraft pulp because it is produced cost-effectively by the pulp and paper industry (Nanko et al. 2005), is readily available in large quantities, and consists mostly of cellulose (> 80%) (Agarwal et al. 2013).

Characterization of CNCs is important because their properties depend on their structural characteristics. For instance, analysis of morphology is important as it tells about the surface area available for physicochemical interactions and surface chemistry (e.g., how many hydroxyl groups available to reactants). CNC morphology affects the distribution of the particles; e.g., in a composite film, which in turn affect the processability and quality of dispersion. Similarly, crystallinity and crystallite size have influence on the important physical properties of CNCs. With increase in crystallinity, tensile strength, dimensional stability, and density increase, while properties such as chemical reactivity and swelling decrease. Measurement of accessibility to water is important for CNC properties that are moisture sensitive, e.g. swelling, film thickness, and water vapor permeability.

The type of CNCs influences mechanical properties of their bio-nanocomposite product (Jorfi et al. 2013). Although structural characteristics and properties of some CNCs have been compared (Guo and Catchmark 2012; Foster et al. 2018; Dunlop et al. 2020), investigation of their supramolecular structures is lacking. Given that there are significant differences in cellulosic starting materials (e.g., degree of polymerization, crystallinity, and fibril size), it is expected that differences would be carried over to CNCs' supramolecular structures.

Whereas H-bonds and weak van der Waals forces are the primary determinants of structure, an assembled supramolecular state has contributions from more variables including fibril size, arrangement of the cellulose chains within the fibril, local conformation of the CH_2OH group, and the types of intra- and interchain H-bonds. Moreover, certain aspects of CNCs also depend upon method of preparation (Mao et al. 2017; Mokhena and John 2020). Accordingly, this work uses only CNCs produced using 48–64% sulfuric acid (S-CNCs), which have sulfated surface primary hydroxyl groups (CH_2OH) resulting in negatively charged nanocrystals of various sizes from the different cellulose substrates.

Crystallinity (CrI) is the principal property used to evaluate CNC supramolecular structure, however its measurement poses difficulties because different methods give different values. XRD—the most often used method—is also very dependent upon how the data are processed (Park et al. 2010). Moreover, different methods seem to be measuring different things. For example, XRD and MAS-NMR measurement of CrI depends upon sample moisture (Agarwal et al. 2017; Wormald et al. 1996). Therefore, to adequately define the supramolecular structure, additional measurements are required.

In this investigation CNCs were produced by 48–64% sulfuric acid hydrolysis of poplar wood, kraft pulp, cotton MCC, bacterial cellulose, tunicin, and cladophora cellulose. Those from bacterial cellulose and tunicin were produced in the acid sulfate form, all others were in the sodium salt form; both forms have identical supramolecular structure. CNCs were analyzed using ICP-OES, TEM, TGA, Raman, MAS-NMR, and XRD with the objective to develop information on their molecular structure. Additionally, accessibility to water (A_{water}) (Agarwal et al. 2016; Agarwal 2017; Foster et al. 2018), exocyclic CH_2OH conformation ratio (Agarwal et al. 2016), and chain conformation disorder (CCONDIS) were measured. Unlike the first two Raman methods mentioned above, the CCONDIS was used to develop information on cellulose chain conformational disorder. The method is based on the ratio of the intensities of two cellulose Raman bands, 900 and 1096 cm^{-1} or I_{900}/I_{1096}. The intensities of both these bands are affected by the conformational disorder present in cellulose samples. A totally amorphous cellulose sample is used as a standard of being 100% disordered.

Materials and methods

Chemicals and materials

NaOH (AR grade) and sodium chlorite (technical grade) were obtained from Sigma–Aldrich (St. Louis, MO) or Alfa Aesar (Tewksbury, MA). Sulfuric acid (Certified ACS plus, 96% assay) and acetic acid (glacial) were from Fisher Scientific (Pittsburg, PA). Cotton MCC (Whatman CC31) was from Whatman International Ltd., (Maidstone, UK). Amorphous cellulose was generated by grinding cotton MCC in a vibratory mill using steel balls for 120 min, as described earlier (Agarwal et al. 2010). All other chemicals and reagents, unless stated otherwise, were purchased from Sigma–Aldrich (St. Louis, MO).

Poplar wood was available at Forest Products Laboratory, Madison WI. Mixed hardwood bleached kraft pulp was obtained from NewPage Corporation, Miamisburg, Ohio. Bacterial cellulose was produced in the laboratory of one of the coauthors at Penn State University (University Park, PA) using a previously published method (Chi and Catchmark 2017). Before acid hydrolysis, the lab-produced bacterial cellulose was purified twice using 0.1 M NaOH at 80 °C for 1 h. Subsequently, the cellulose pellicles were rinsed with deionized water until the pH reached neutral and then freeze dried. Tunicates (Styela clava) were collected from floating docks in Brest, France. Cladophora, a highly crystalline algae, was collected from Lake Mendota in Madison, WI.

CNC production

Most of the CNCs were produced using previously published methods: hydrothermally treated poplar wood (Agarwal et al. 2018a), kraft pulp (Agarwal et al. 2016; Reiner and Rudie 2013), cotton MCC and cladophora (Agarwal et al. 2016, 2018a), bacterial (see below), and tunicin (Jorfi et al. 2013). CNCs from bacterial cellulose and tunicin were produced in the acid form from 48% and 60% H_2SO_4 respectively, all others were as sodium salts from 64% H_2SO_4. For bacterial CNCs the method of Hirai et al. (2009) was used with minor modifications as follows. To produce CNCs, the lyophilized bacterial cellulose was treated with 48 wt% sulfuric acid at 70 ml/g for 2 h at 45 °C. Then the suspension was diluted tenfold to stop the reaction, after which the suspension was centrifuged,

decanted and washed once with deionized water and then centrifuged again. The centrifuge step was repeated at least three times until the supernatant became turbid. The supernatant was then collected and dialyzed (3.5 K molecular cut off) against deionized water for several days until constant pH. Finally, to remove any aggregates, the suspension was sonicated (Branson Model 5510, Danbury) under ice-bath cooling for 10 min.

Transmission electron microscopy (TEM)

For TEM analysis of the CNCs, carbon grids (300 mesh) were floated on diluted sample droplets for $\sim$ 1 min, then rinsed through stain (2% aqueous uranyl acetate) and blotted dry. Samples were imaged using a Philips CM-100 TEM operated at 100 kV, spot 3, 200 µm condenser and 70 µm objective apertures. Images were captured in digital form using Orius SC200-1 2 Mpixel CCD camera (Gatan, Inc., Pleasanton, CA). Dimensions of at least 100 particles for each type of CNCs were measured, excluding both large clumps suspected of being aggregates of drying and small clusters, using the open source program Image J (Program ImageJ). When possible a straight line was chosen, otherwise a 4–6 segmented option was used for long, kinked specimens. Length and width data were subjected to pairwise t-tests at $p = 0.05$ using Microsoft Excel to determine if the CNCs were statistically different.

Sulfur analysis

CNC samples were analyzed for sulfur content using an ICP-OES spectrometer Horiba (Edison, NJ) ULTIMA II with 12 L/min plasma gas, 0.2 L/min sheath gas, 0.28 L/min nebulizer gas and a 20 µm/15 µm slit combination. Measurements were the average of 3 replicate readings in max mode with 0.5 sec integration time. Calibration used a 7-point, linear external standardization with correlation coefficient > 0.999 for line 180.676 nm.

Thermogravimetric analysis (TGA)

The thermal properties were measured using a thermogravimetric analyzer, Perkin Elmer TGA 7 (PerkinElmer Inc., Waltham, MA). The TGA measurements were carried out in the temperature range 50 to 700 °C at a heating rate of 10 °C/min under N_2 atmosphere (20 mL/min).

Analysis by Raman spectroscopy

The CNCs and the starting materials were analyzed, in triplicate, with a Bruker (Billerica, MA) MultiRam equipped with a 1064-nm 1,000 mW continuous wave (CW) diode pumped Nd:YAG laser. Spectra were recorded from 2048 or 4096 co-added scans using 600 mW laser excitation, as reported previously (Agarwal et al. 2016).

For estimations of crystallinity (Agarwal et al. 2010, 2013, 2018b) and exocyclic CH_2OH conformation ratio (Agarwal et al. 2016) sample pellets were prepared with a pellet-forming die using a force of 276×10^6 dyn/cm^2 compressive pressure. For "accessibly to water" analysis (Agarwal et al. 2016; Agarwal 2017; Foster et al. 2018) sampling in H_2O and D_2O was done in shortened MAS-NMR tubes using a previously reported method for the complete OH-to-OD exchange (Agarwal et al. 2016). For "chain conformation disorder or CCONDIS analysis" spectra were obtained in both freeze-dried and wet (in water) states. Briefly, spectra of approximately 25 mg of dry sample in a shortened MAS-NMR tube were measured. Then, for the wet analysis, a small amount (0.2 mL) water was added to the sample and centrifuged at 4000 rpm for $\sim$ 1 min so that the wetted sample settled to the bottom of the tube and then was re-analyzed. In all cases, Bruker OPUS 7.2 software was used to process the spectral data which involved normalization, selection of a spectral region, background correction, and band integration. Background correction was performed using a 64 points OPUS "rubberband option". For plotting purposes, the spectra were converted to ASCII format and exported to Excel.

Crystallinity by Raman spectroscopy

Cellulose CrI was estimated using two methods—380-Raman (Agarwal et al. 2010, 2013) and 93-Raman (Agarwal et al. 2018b). The following two equations were used to estimate these CrIs.

$$\mathrm{CrI}_{380-\mathrm{Raman}} = \frac{\left(\left(\frac{I_{380}/I_{1096})-0.0286)}{0.0065}\right) + 2.0212\right)}{0.8222} \quad (1)$$

$$CrI_{93-Raman} = \frac{\left(\frac{I_{93}}{I_{1096}}\right) - 0.0182}{0.0029} \quad (2)$$

Accessibly to water

Calculations were based on the intensity increase of the Raman 1380 cm^{-1} band after the sample underwent complete OH-to-OD exchange. The following equation was used to estimate accessibility to water (A).

$$A(Raman) = \frac{\Delta I_{1380}(CNC) * 100}{\Delta I_{1380}(amorphous)} \quad (3)$$

where ΔI_{1380}(CNC) is the change in the relative intensity of the 1380 cm^{-1} band (relative to 1096 cm^{-1}) of cellulose in the Raman spectrum of a CNC that resulted upon a complete OH-to-OD exchange. Similarly, the value in the denominator is for a completely amorphous sample. More details have been described previously (Agarwal et al. 2016; Foster et al. 2018).

Exocyclic *gt/tg* CH_2OH conformation (ratio 1460/1480)

The I_{1460}/I_{1480} ratio was calculated to estimate the *gt/tg* conformation present in the CNCs using a previously described method (Agarwal et al. 2016). To calculate intensities for the 1480 and 1460 cm^{-1} bands, the ''two baseline points'' method was selected using 1441 and 1500 cm^{-1}, then a sloping baseline was drawn between these points and peak heights at 1460 and 1480 cm^{-1} were measured from the baseline.

Chain conformation disorder (CCONDIS)

In this investigation, a new method based on cellulose's 900 cm^{-1} Raman band was developed to measure the chain-conformational disorder (CCONDIS) that existed in the cellulose nanomaterials. Briefly, the method is based on first measuring, with respect to 100% amorphous cellulose (which is known to be completely disordered from the perspective of cellulose chain conformation), the amount of the disorder that exists in a sample. For CNCs, the disorder is calculated by measuring intensity of the 900 cm^{-1} Raman band (relative to 1096 cm^{-1} intensity) and then dividing it by the relative intensity of the 900 cm^{-1} peak in the spectrum of the completely amorphous cellulose (100% chain disordered material), as shown in Eq. 4 below. Based on earlier analysis of this material (Agarwal et al. 2010), a long duration (120 min) ball milled cotton MCC sample was selected as completely amorphous cellulose. Using Eq. 4 the % CCONDIS was calculated for freeze-dried and never-dried\wet CNCs. In the 1096 cm^{-1} normalized spectra, heights were calculated using OPUS 7.2 and "one base line point method". For the 900 cm^{-1} peak, the latter involved choosing a minimum intensity wavenumber near the peak (855 cm^{-1} was chosen) and drawing a horizontal line under the peak from that wavenumber. Subsequently, the peak height was measured from this horizontal line. Similarly, peak height was also measured for the 1096 cm^{-1} band of cellulose (Agarwal et al. 2016).

$$CCONDIS = \frac{\left(\frac{I_{900}}{I_{1096}}\right) CNC * 100}{\left(\frac{I_{900}}{I_{1096}}\right) amorphous} \quad (4)$$

X-ray diffraction and crystallinity estimation

Wide-angle X-ray diffraction (XRD) profiles were recorded at the Materials Research Science and Engineering Center, University of Wisconsin, Madison using a Bruker (Billerica, MA) D8 Discover diffractometer in reflection mode with 0.5 mm beam aperture and equipped with monochromatic CuKα (λ = 1.5418 Å) point source and a VÅNTEC-500 detector. The X-ray diffractometer beam aperture of 0.5 mm was used. In all cases, diffractograms were obtained on the same samples (in pellet form) that were previously analyzed by FT-Raman spectroscopy. In XRD, both sides of the pellet were sampled and average values of the CrIs are reported.

XRDs were deconvoluted, withing the 2θ ranges of 7° to 37°, using a combination of five pseudo-Voigt profiles and a line. It has been reported that compared to other functions pseudo-Voigt functions perform better (Wada et al. 1997). This XRD range contained all the significant scattering peaks of cellulose. The overall profiles consisted of four crystalline components, representing the (1–10), (110), (200), and (004)

peaks, and one amorphous profile. A total of sixteen different fitting parameters were used. These included scale (5), mean position (5), variance (2), mixing parameter (2), line slope (1), and line intercept (1) parameters. The scale and 2θ position for each of the pseudo-Voight profiles was independently refined. The mixing parameter and variance could vary but were needed to be identical for all the crystalline profiles. All fitting parameters were restricted to ensure the resulting fit had physical meaning. Examples of this are, bounding 2θ positions within specific ranges and not allowing negative scale or variance parameters. CrIs were calculated by using the ratio of the crystalline profiles area to the combined area that included, in addition, the amorphous component. The combined area did not include the line background area because it can arise due to non-sample factors (Yao et al. 2020).

MAS-NMR crystallinity

The C4 spectral region of the ^{13}C MAS-NMR spectra was used to determine the degree of crystallinity of the samples. In NMR, signals of the crystalline and non-crystalline cellulose are detected, respectively, in 87–91 and 82–86 ppm regions. Since the MAS-NMR spectra were recorded on dry samples the resolution of the non-crystalline C4 region (about 86–79 ppm) was, as expected, poor. For this reason, the spectral fitting of the non-crystalline region was performed for the sole purpose of obtaining a reasonable fit in a least-squares sense.

The crystalline and non-crystalline C4 regions are separated by a signal intensity minimum, which is quite shallow minimum in some spectra. The division of fitted functions into "crystalline" and "non-crystalline" was made based on their peak positions relative to this signal intensity minimum. Fitted functions with positions at a chemical shift value larger than the signal intensity minimum were considered to originate from "crystalline" structures, and vice versa.

The degree of crystallinity (Eq. 5) was calculated as the ratio of the fitted signal intensity from the crystalline region (A_c) divided by the total fitted signal intensity, contributions of both A_c and A_a (amorphous), from the whole of the spectral C4-region. More details can be found in the literature (Larsson et al. 1997)

$$CrI_{NMR} = \frac{A_c * 100}{(A_c + A_a)} \quad (5)$$

Lateral fibril dimension

Lateral fibril dimensions (LFDs) (based on q in Eqs. 6–7) of the CNCs were calculated from the fraction of the C4 signal intensity from accessible and inaccessible surfaces (q).

$$q = (Ias + IIas)/ITot \quad (6)$$

I_{Tot} is the total signal of C4, I_{As} and I_{Ias} are the signal of accessible and inaccessible CNC surfaces respectively. Moreover, there is an experimental relationship between q and n.

$$\mathrm{q} = \frac{(4n-4)}{n^2} \quad (7)$$

In this equation, n is the number of cellulose polymers perpendicular to the CNC cross-section along one side of the assumed square CNCs. A conversion factor of 0.57 nm per cellulose polymer has been calculated as the mean value of the repeat distance of cellulose chains in the wide (0.61 nm, monoclinic 110 and triclinic 010) and narrow (0.54 nm, monoclinic 1–10 and triclinic 100) surfaces (Hult et al. 2001). The mean value is used since in the case of the inaccessible surfaces, no assignment can be made to the specific forms, in contrast to the accessible surfaces (Wickholm et al. 1998).

$$LFD = 0.57 \times n \quad (8)$$

Tg/gt ratio by NMR

NMR spectra in the C6 region (58–68 ppm) were used to estimate the *tg*/*gt* ratio of the exocyclic CH_2OH group. The tg and gt conformation were represented by peaks at 65 and 62 ppm positions, respectively. For the 65 ppm peak, the peak area was calculated by drawing a horizontal line under the peak from 68 ppm and integrating the area between 67 and 63 ppm. Analogously, the area of the 62 ppm signal was estimated by drawing a horizontal line under the band from 59 ppm and integrating the intensity between 59 and 63 ppm.

Results and discussion

"Results and discussion" section is organized into the following six main sections—morphologies, sulfur content and degradation temperature, crystallinities of the CNCs, other supramolecular state parameters, sulfated vs. non-sulfated kraft pulp CNCs, and MAS-NMR analysis. However, the "crystallinities" section contains a subsection "crystallinities in wet state" and "the other supramolecular state parameters" section consists of three additional sub-sections, namely, "accessibility to water", "exocyclic *gt*/*tg* CH_2OH conformation", and "chain conformational disorder (CCONDIS)".

Morphologies

Transmission electron micrographs (TEMs) of the various types of CNCs are shown in Fig. S1, a–f. These were obtained from poplar (Fig. S1a), kraft pulp (Fig. S1b), cotton MCC (Fig. S1c), bacterial (Fig. S1d), tunicin (Fig. S1e), and cladophora cellulose (Fig. S1f). Their morphological data—average lengths, widths, and the aspect ratios—are reported in Table 1. Based on this information, the CNCs can be broadly categorized into two groups: those having the aspect ratio > 30 and < 12. Tunicin, cladophora and bacterial cellulose CNCs belonged to the former category, whereas the rest of the CNCs belonged to the < 12 set. These TEM measurements are in agreement with measurements of similar CNCs reported by other investigators (Moon et al. 2011; Sacui et al. 2014; Elazzouzi-Hafraoui et al. 2008).

Among the members of the aspect ratio < 12 set (poplar, kraft pulp, cotton MCC) the level-off degree of polymerization, or LODP values, are very similar (216 to 256, estimated from the avg. length based on 2 glucose units /nm; Table 1) though their starting material crystallinities were quite different (Table 2). This suggests that these materials have frequently-occurring non-crystalline regions along the cellulose fibrils where the acid hydrolysis takes place. By contrast, the aspect ratio > 30 set (tunicin, cladophora and bacterial cellulose) have significantly larger distances between the non-crystalline regions, which would explain both their large crystallite size (Agarwal et al. 2016, 2017) and high CrIs of the starting materials (Table 2).

Sulfur content and degradation temperature

Information on sulfur content and degradation temperature (DTG, based on TGA) of the CNCs are reported in Table 1. Sulfur content of the analyzed samples was as expected for CNCs produced by 48–64% H_2SO_4 hydrolysis and indicated that all the CNCs contained surface sulfate half-ester groups. CNCs from tunicin and bacterial cellulose had, respectively, the most and least amount of such groups (Table 1). The reason for this is likely to be that compared to tunicin a lower concentration of the acid (48%) was used for the hydrolysis. Dependence of sulfation level on the acid concentration is known (Chen et al. 2015).

To compare the thermal stability of the CNCs, TGAs were obtained and the temperature of maximum

Table 1 Dimensions of the CNCsa

CNC sample	Avg. length, nm	Avg. width, nm	Aspect ratio	Sulfur content, wt%	Degradation temperature (DTG), °C
Poplar[b]	108 ± 43	10 ± 3	10.7	0.87	328
Kraft pulp	123 ± 58	11 ± 4	11.5	1.1	322
Cotton MCC	128 ± 40	13 ± 4	9.8	0.87	286
Bacterial cellulose[c]	795 ± 410	8.2 ± 2.4	97	0.14	303
Tunicin	1300 ± 783	25 ± 8	52	1.6	417
Cladophora cellulose	1008 ± 399	33 ± 7	31	0.50	364

[a]Except bacterial and tunicin CNCs which were in the acid sulfate forms, others contained the sodium sulfate groups; [b]Hydrothermally treated at 170 °C; [c]except DTG all other data from Chi and Catchmark 2017

Table 2 Percent cellulose crystallinities of the air-dried (25° C) starting materials

Materials	380-Raman	93-Raman	XRD	MAS-NMR
Poplar	55.5	41.3	62.7	47.6
Kraft pulp	53.2	36.7	75.0	38.1
Cotton MCC	82.2	74.7	83.5	66.3
Bacterial cellulose	65.6	53.9[a]	69.8	68.7
Tunicin	86.5	128.4[b]	83.8	89.8
Cladophora cellulose	82.5	63.4[a]	73.0	76.4[c]

[a]Shows a broader band compared to tunicin; [b]Higher than 100% due to the limitation of the calibration used to evaluate 93-Raman CrI (a tunicin sample was not included in developing the calibration—Agarwal et al. 2018b); [c]In MAS-NMR, a different aliquot of cladophora sample was used which had slight impurity

degradation rate (DTG) were obtained (Table 1). The thermal degradation varied between 286 °C and 417 °C, with tunicin CNCs being most stable and cotton MCC CNCs least stable. However, thermal stability data should be interpreted after considering that samples showed variation in %S content and that two of the sulfated CNCs were in the acid form (bacterial and tunicin). It has been reported that, compared to the non-sulfated and sodium salt forms, the free acid form degrades more easily (Lin and Dufresne 2014; Wang et al. 2007). Additionally, in acid form, CNC surface charge density was found to be the determining factor in thermal stability due to de-esterification and acid-catalyzed degradation (Vanderfleet et al. 2019); conversely, in sodium form the surface chemistry and charge density had a negligible effect on the onset of thermal degradation, but DP of the cellulose polymer chains highly influenced stability (Vanderfleet et al. 2019). Here, however, the tunicin CNCs in acid sulfate form had the highest DTG of 417 °C and also the highest %S (1.6%, Table 1). This suggested that %S is not the predominant factor, rather CrI (Table 3) and/or the aspect ratio (Table 1) may be more important because both were significantly higher for tunicin CNCs.

Crystallinities of the CNCs

In general, the aggregated states of cellulose materials remain poorly understood largely due to the fact that this natural polymer can exist in many crystalline (e.g., crystalline forms I, II, III, and IV) and non-crystalline organizations (Agarwal et al. 2018b). The impact of the latter organizations on cellulose crystallinity estimations is an open question (Park et al. 2010; Lindner et al. 2014; Agarwal et al. 2016, 2018b). Nevertheless, crystallinity measurement is widely used to assess the nature of the aggregated state although the methods used have significant limitations (Agarwal et al. 2010; Park et al. 2010, Agarwal et al. 2018b). Additionally, in XRD, it was reported that the CrI value of cellulose materials depended upon moisture content where, in general, CrI was higher in the wet state as compared to the dry state. This was particularly true for low crystallinity materials (Agarwal et al. 2017).

The CrIs of the six CNCs were estimated by Raman (93-Raman and 380-Raman), XRD (deconvolution), and MAS-NMR methods (Table 3). As an example, estimation of the XRD CrI by deconvolution is shown in Fig. S2 for the pulp CNCs. Of the two Raman

Table 3 Percent crystallinities and lateral fibril dimensions of the CNCs

	380-Raman	93-Raman	XRD	MAS-NMR	LFD[a], nm
Poplar	62.0	55.9	82.0	57.5	4.1
Kraft pulp	55.5	46.4	74.9	51.8	4.7
Cotton MCC	77.1	67.9	89.4	65.8	6.0
Bacterial	77.3	79.0	85.4	72.2	7.6
Tunicin	69.9	92.8	81.1	86.8	16.7
Cladophora	72.1	58.1	75.7	92.3	29.2

[a]Lateral fibril dimension (LFD) by MAS-NMR

methods used, 380-Raman and 93-Raman, the difference is as follows. When organized/ordered cellulose is present in a sample along with or in lieu of crystalline cellulose, 380-Raman method classifies this non-crystalline form as crystalline whereas that is not the case with 93-Raman method (Agarwal et al. 2018b). The latter method ignores the contribution of non-crystalline cellulose and only measures the crystalline phase. However, because this continues to be a topic of ongoing research, in the present investigation, both the measurements are included.

Comparing crystallinities of the CNCs with starting materials, both the 380-Raman and 93-Raman CrIs increased for wood, pulp, and bacterial cellulose and decreased for cotton MCC, tunicin and cladophora (Tables 2, 3). XRD CrIs also increased for wood, cotton MCC, and bacterial cellulose CNCs, but showed little or no change for pulp, tunicin, and cladophora CNCs (Tables 2, 3). By contrast, MAS-NMR showed a large increase for cladophora as well as for wood and pulp, a small increase for bacterial cellulose and a very small decrease for cotton MCC and tunicin.

What are the reasons for such variable trends between methods and, importantly, why do the CrIs not increase for all samples upon CNC production? Additionally, in the case of lower crystallinity starting materials (wood, pulp, and bacterial cellulose), why is not the CrI increase significantly higher—because the acid hydrolyses most of the disordered/non-crystalline cellulose and, consequently, should leave only highly crystalline cellulose?

Considering the mild nature of the acid hydrolysis conditions, changes to the crystallite size upon CNC production is not likely and therefore, can be ruled out. Shortening of the fibrils and retaining of the disorder in the CNCs are plausible explanations. An additional possibility, in the case of poplar and pulp CNCs, is that their tapered ends may be non-crystalline; however, this is not important for cladophora and tunicin CNCs which have significantly larger dimensions (Table 1, Fig. S1e and Fig. S1f).These considerations provide impetus for future work and comparative analysis of measurement methodologies.

Table 4 Percent crystallinities of the CNCs in dry and wet states

Sample	380-Raman		MAS-NMR	
	Dry	Wet	Dry	Wet
Poplar	62.0	58.0	57.5	62.7
Kraft pulp	55.5	53.3	51.8	57.7
Cotton MCC	77.1	62.7	65.8	72.9
Bacterial	77.3	75.7	72.2	76.5
Tunicin	69.9	74.7	86.8	85.5
Cladophora	72.1	80.2	92.3	92.3

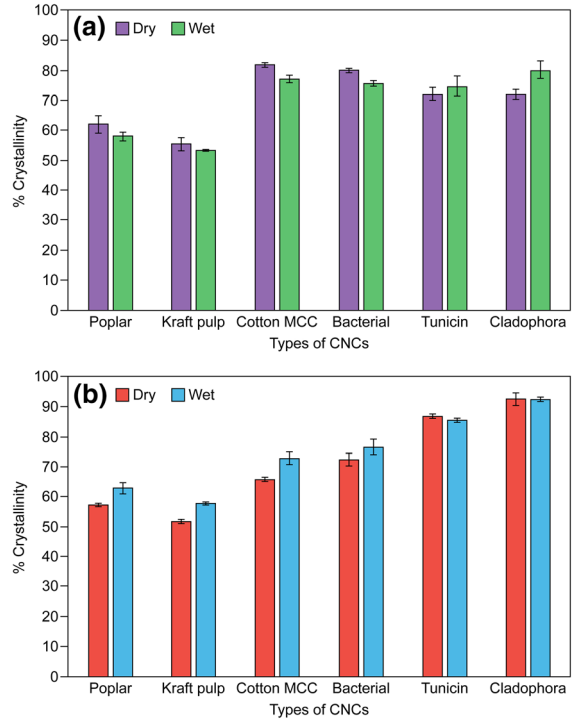

Fig. 1 Crystallinities of the CNCs in dry and wet states (**a**) 380-Raman and (**b**) ^{13}C MAS-NMR

Crystallinities in wet state

To find out CrIs of the CNCs in the wet state, 380-Raman and MAS-NMR methods were used because both the methods can provide such information (Table 4). Figure 1a and b compare the dry- versus wet-state crystallinities (Table 4) estimated by 380-Raman and MAS-NMR methods, respectively, and clearly show the opposite impact of water in these

methods. For low crystallinity samples (poplar, kraft pulp, cotton MCC, and bacterial cellulose) the wet-state 380-Raman CrIs were lower, whereas MAS-NMR CrIs were higher. By contrast, for higher crystalline samples (tunicin and cladophora) the 380-Raman CrIs increased slightly in wet state, while the MAS-NMR CrIs remained unchanged. The reason for such changes is likely to be reorganization of cellulose chains in non-crystalline regions (including crystallite surfaces) when the chains interact with water molecules. The improved alignment of the chains impacts various Raman bands (Fig. S3), especially affecting the intensities at 380 cm^{-1} and 1096 cm^{-1}. In 380-Raman, the change will depend upon which of the two peaks (1096 and 380 cm^{-1}) involved in the CrI determination increases more upon water-induced reorganization. MAS-NMR signals of the crystalline and amorphous C4 at 79–91 ppm are also impacted, however the effect of chain reorganization is opposite due to the way CrIs are calculated in these different methods (Agarwal et al. 2010, 2013 and Larsson et al. 1997). Moreover, the extent of the effect depended upon the CNCs' dry-state CrI, which varied significantly among this sample set (Table 3). The observations and trends in this study, as calculated by the Raman methods, are consistent with the "non-crystalline cellulose reorganization" explanation previously invoked by Agarwal et al. (2017). There the authors used it to explain the moisture-induced changes in X-ray diffraction patterns of various cellulose materials, and the explanation is plausible given the strong interaction of cellulose with water.

Other supramolecular state parameters

Traditionally, CNC crystallinity has been the primary measurement used to assess the aggregated state. However, accessibility to water (A_{water}) (Agarwal et al. 2016; Agarwal 2017; Foster et al. 2018), exocyclic *gt*/*tg* CH_2OH conformation ratio (Agarwal et al. 2016), and chain conformational disorder (CCONDIS)—all based on Raman spectroscopy—are additional measurements pertinent to describing the supramolecular state of CNCs. Of the four Raman spectroscopy-based measurements, two were developed for the first time in the context of understanding the supramolecular state of cellulose in never-dried woods (Agarwal et al. 2016) and are also potentially useful for characterizing CNCs. The Raman methods for estimating cellulose crystallinity were developed in the corresponding author's laboratory (Agarwal et al. 2010, 2018b). In the present investigation a Raman method for measuring CCONDIS is developed.

Accessibility to water

The highest and lowest values of accessibility to water (A_{water}) were those from pulp and cladophora CNCs, respectively (Table 5; Fig. 2). The highest value was 11.5 times greater than the lowest A_{water}, with the variability likely dependent upon structural factors such as a crystal's lateral dimension and crystallinity. Because the A_{water} measurement is based on availability of the OH in CH_2OH for conversion to CH_2OD, a larger surface area (i.e. smaller crystals) (Brinkmann et al. 2015) results in higher A_{water}. Accordingly, comparing the two highly crystalline CNCs (tunicin and cladophora), the wider cladophora CNCs with higher LFD value (Table 3) showed significantly lower A_{water}, consistent with fewer exocyclic CH_2OH groups for the OH-to-OD exchange. Considering crystallinity as an influencing factor for A_{water}, low order/crystallinity provides accessibility to internal CH_2OH groups so they can also be converted to CH_2OD.

Exocyclic *gt*/*tg* CH_2OH conformation

The exocyclic *gt*/*tg* CH_2OH conformation ratios were calculated from the Raman spectra of the CNCs (Table 5). In a perfect crystal situation, the *gt*-conformation is expected to be present only on the surface of the crystals because in the crystalline phase all the CH_2OH conformation is presumed to be *tg* type (Nishiyama et al. 2002; Agarwal et al. 2016). Raman spectra in the CH2 bending region (1440–1500 cm^{-1}) shown in Fig. 3 show significant differences in the band intensities among the CNCs. Ratios I_{1460}/I_{1480} were calculated (Table 5) and are plotted (Fig. 4). Data exhibited significant variation (0.38 to 0.62) indicating significant conformational differences between the CNCs.

Another point to note is that the 1460/1480 ratio is only a modest way to ascertain conformational differences; a more complex picture emerges from

Table 5 Comparison of Raman spectroscopy derived supramolecular state parameters

Sample	CNCs A_{water} (%)	Exocyclic *gt/tg* CH_2OH conformation, I_{1460}/I_{1480}		Chain conformational disorder of CNCs, CCONDIS (%)	
		CNCs	Starting material	Wet	Freeze-dried
Poplar	21.8	0.52	0.70	22.4	37.2
Kraft Pulp	25.3	0.62	0.71	23.0	41.4
Cotton MCC	9.5	0.40	0.44	17.5	24.0
Bacterial cellulose	5.8	0.45	0.54	16.9	21.4
Tunicin	11.6	0.37	0.36	15.3	19.2
Cladophora cellulose	2.2	0.52[a]	ND[b]	10.7	22.2

[a]Raman spectrum had some fluorescence which can introduce some error;

[b]Not determined

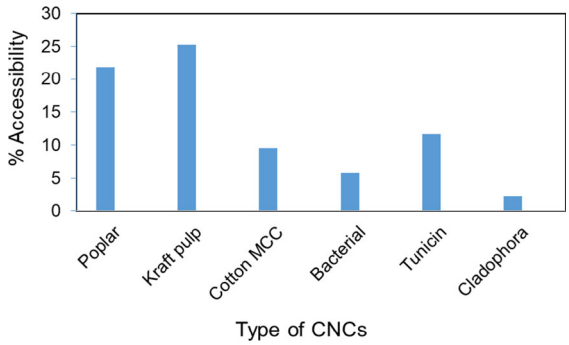

Fig. 2 CNCs accessibility to water

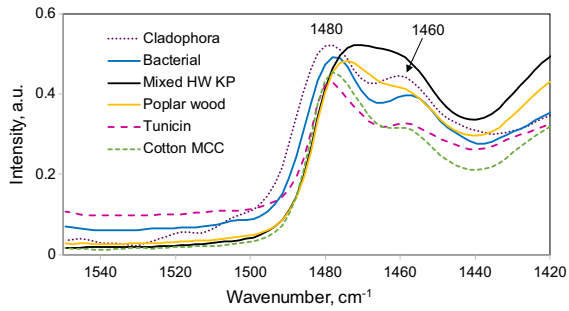

Fig. 3 CH_2 bending mode bands in the exocyclic CH_2OH conformation (*tg* and *gt*) region in the Raman spectra of the CNCs

examination of the spectra (Fig. 3). As an example, both poplar and cladophora CNCs have I_{1460}/I_{1480} ratio of 0.52 (Table 5) but examination of the spectra demonstrates the cladophora CNC had significantly

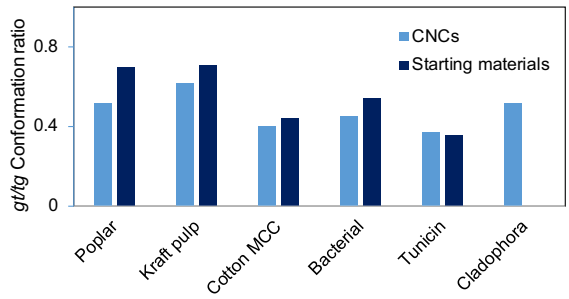

Fig. 4 *gt/tg* CH_2OH conformation ratios of CNCs and starting materials, based on Raman bandintensity ratio (I_{1460}/I_{1480})

higher *tg* content (Fig. 3) as the two bands were better resolved.

It is possible that differences in 1460/1480 intensity ratios cannot be attributed entirely to differences in surface (exocyclic *gt/tg*) CH_2OH group content; in which case, the implication is that supramolecular structures of the CNCs differed significantly. To investigate this further, the 1460/1480 ratios of the starting materials were compared to their CNCs (Fig. 4), except for cladophora for which reliable *gt/tg* ratio could not be calculated due to fluorescence in its Raman spectrum.

Because acid hydrolysis removes less ordered cellulose, CNCs exhibit lower band intensity of the 1460 cm^{-1} peak. Considering that CNCs had only slightly lower 1460/1480 ratios than their raw materials, we conclude that the disorder originally present in the starting materials is significantly preserved in the CNCs, especially for poplar and pulp with low

crystallinity CNCs. This is especially true because the small decline in the ratio can be attributed to the contribution of the hemicelluloses present in the starting materials which were, for the most part, removed upon the acid hydrolysis.

Chain conformational disorder (CCONDIS)

CCONDIS measurements were based on the Raman cellulose intensity ratio 900 cm^{-1}/1096 cm^{-1}, with 120-min ball-milled cotton MCC taken to have 100% disorder. The intensities of both these bands I are impacted due to conformational disorder (Agarwal et al. 2010)—whereas, with the increased disorder, the intensity at1096 cm^{-1} declines, at 900 cm^{-1} it increases. Tunicin was selected as a high crystalline cellulose sample for comparison. Crystallinities of these materials were previously analyzed by Raman and XRD methods (Agarwal et al. 2010, 2016) and support their use for the present purpose. In the 1096 cm^{-1} normalized spectra, tunicin (Fig. S4) exhibited very low intensity at 900 cm^{-1} (Fig. S4), whereas the completely amorphous ball-milled cotton MCC exhibited very strong intensity (Fig. S4 and Fig. S5). Use of the 900/1096 cm^{-1} peak ratio as a gauge of conformational order is further supported by the plots in Fig. S5 where 1096 cm^{-1} normalized spectra are plotted for cotton MCC samples that were ball milled for various durations (Agarwal et al. 2010). Clearly, compared to shorter duration ball milled samples, longer duration ball milled samples produced higher intensity 900 cm^{-1} peak which in turn implied that such celluloses were increasingly more disordered. It is well known that ball milling de-crystallizes cellulose and introduces chain disorder (Howsmon and Marchessault 1959; Agarwal et al. 2010; Ling et al. 2019).

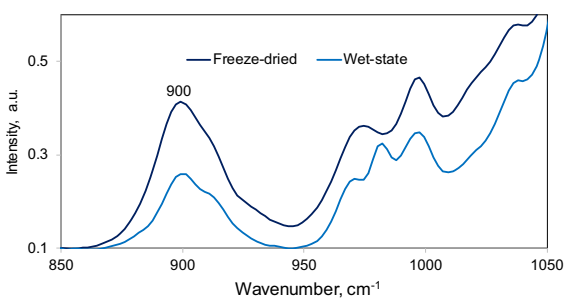

Fig. 5 1096 cm^{-1} normalized Raman spectra of kraft pulp CNCs in wet-state and freeze-dried state

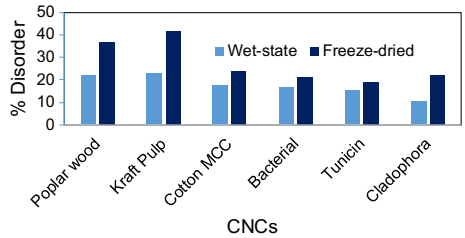

Fig. 6 Chain conformational disorder of the CNCs

For the CNCs, chain disorder was measured by first calculating the height of the 900/1096 ratio and then assigning it a value based on the 900/1096 ratio in the spectrum of the 100% disordered cellulose (Eq. 4). Disorder (called chain conformational disorder or CCONDIS) was calculated for both wet- and freeze-dried states of the CNCs (Table 5; Fig. 5). Wood and pulp CNCs had higher disorder, which was significantly increased upon freeze-drying. Other freeze-dried CNCs also showed higher CCONDIS compared their wet state. Given cellulose's affinity towards water, this is not surprising because wetted cellulose chains have heightened ability to reorganize to become more aligned (higher order/organization), which is reflected in lower 900/1096 ratio (Fig. 6) thereby demonstrating the utility as a measure of CCONDIS.

It is clear that in the wet-state cladophora and tunicin CNCs had the least amount of the disorder whereas wet-state pulp CNCs had the most. Previous investigation of pulp CNCs by MAS-NMR reported the existence of such disorder, with a distribution of environments distinguished by their structure and crystalline perfection (Lemke et al. 2012).

Upon freeze drying, all the CNCs became more disordered but pulp CNCs had the highest disorder (Table 5; Fig. 6). Interestingly, in the freeze-dried state, CNCs produced from hydrothermally treated poplar had about 33% lower disorder compared to pulp CNCs. Although the disorder introduced upon freeze drying can come from several sources, one possibility is that molecular water (1–2 water molecules between chains) may act as an "adhesive" or "ordering agent" and allows for chain flexibility (like a plasticizer). These molecules maintain some kind of order in the wet state but when removed upon

Table 6 Comparing kraft-pulp CNCs—sulfated (S-CNCs) versus non-sulfated (CNCs)

Sample	DTG (°C)	Crystallinity (%)		CNCs A_{water} (%)	Exocyclic *gt/tg* CH_2OH conformation ratio I_{1460}/I_{1480}	Chain conformational disorder (CCONDIS) of CNCs (%)	
		XRD	380-Raman			Wet	Freeze-dried
S-CNCs	322	74.9	53.3	25.5	0.62	23.0	41.4
CNCs*	361	71.5	53.4	26.7	0.64	31.8	52.1

*Produced by HCl hydrolysis of the pulp

freeze drying, the chains or chain-fragments become disordered (Fang and Catchmark 2014).

Sulfated versus non-sulfated kraft pulp CNCs

To find out if the sulfation of the CNCs had any impact on the supramolecular properties, especially as determined by Raman spectroscopy, CNCs from kraft pulp were also produced by HCl hydrolysis. For this, the method of Araki et al. (1999) was used with some modifications (Supplementary material). An AFM image of the HCl-CNCs is shown in Fig. S6. The image showed that the CNCs existed in the aggregated form and this seems to have been because the surface charge of the HCl-CNCs is low (Araki et al. 1999).

Various properties and characteristics of the two types of pulp CNCs are compared in Table 6. Although, as expected, the thermal degradation temperature of the non-sulfated CNCs was higher by about 40 °C, the CrIs of the two types of CNCs were similar. Of the three supramolecular characteristics determined by Raman, accessibility to water (A), CH_2OH conformation, ratio (I_{1460}/I_{1480}), and conformational disorder, the data for the first two were alike (Table 6) and implied that the pulp CNCs' sulfation levels of 1.1% did not impact these two characteristics. On the contrary, in both the states (wet and freeze-dried) compared to the sulfated CNCs, the CCONDIS was higher for the non-sulfated nano-crystals. The reasons for this are not clear but may have to do with the differences between the hydrolysis conditions (e.g., acid type, acid concentration, hydrolysis duration). Further research is needed to address such questions.

MAS-NMR analysis

^{13}C MAS-NMR spectra also provide information on the supramolecular structure of celluloses. In an MAS-NMR spectrum, peaks due to C6, C4, and C1 of cellulose molecule appear, respectively, in the 58–68, 79–91, and 101–109 ppm regions. On the other hand, C2, C3 and C5 carbons contribute in the 68–80 ppm region (Atalla and Vanderhart 1984). However, for the

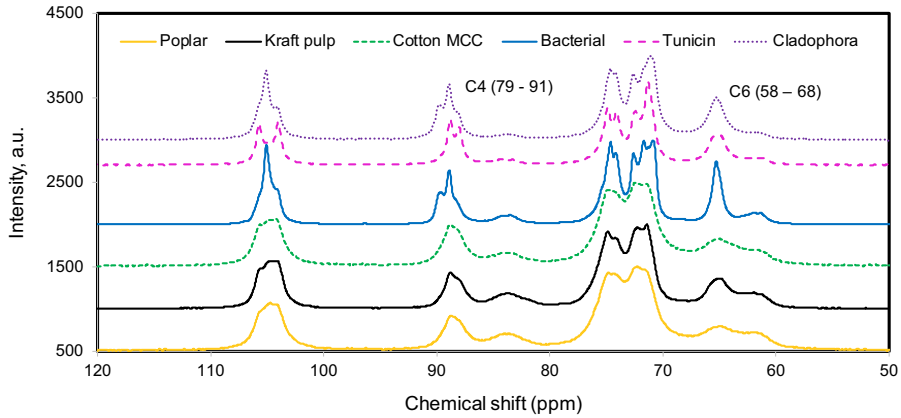

Fig. 7 MAS-NMR spectra of the CNCs. The C4 (79–91 ppm) and C6 (58–68 ppm) regions are annotated

C4 shifts, based on computational analysis, it was reported that a number of factors like conformations of exocyclic groups at C6 (*tg*, *gt*, and *gg*), H_2O molecules H-bonded on the surface of the microfibril, glycosidic bond angles and the distances between H4 and HO3 atoms can affect the C4 shifts (Yang et al. 2018). For the CNCs, such spectra are shown in Fig. 7 where the regions associated with the C4 and C6 carbons are annotated. Earlier, the information from the C4 region in MAS-NMR was used to estimate cellulose crystallinity (Tables 2, 3, 4). It is well known that chemical shift of the C6 carbon in cellulose is influenced by the conformations of exocyclic groups at C6 (e.g., *tg* and *gt*) (Horii et al. 1983). For the bacterial, tunicin, and cladophora CNCs, the *tg* peak ($\sim$ 65 ppm) is significantly higher compared to the *gt* peak ($\sim$ 62 ppm) (Fig. 7). Because high number of *tg* conformation of CH_2OH groups (high *tg*/*gt* C6 ratio) imply highly crystalline materials, these CNCs can be expected to have high crystallinity. This is supported by the crystallinity data in Table 3. On the other hand, the *tg*/*gt* C6 intensity ratio was significantly lower for the poplar, kraft pulp, and cotton CNCs (0.59–1.38, Fig. S7) and therefore, compared to the CNCs from bacterial, tunicin, and cladophora (*tg*/*gt* C6 intensity ratio 2.62–3.57, Fig. S7) they can be expected to have lower crystallinity.

Lateral fibril dimensions (LFDs) were estimated from the MAS-NMR-spectra of the CNCs (Table 3) assuming a square cross-section (Hult et al. 2000). Poplar and pulp LFDs were found to be similar (4–4.5 nm) and significantly lower as compared with tunicin and cladophora (16.7–29.2 nm) (Table 3). The remaining CNCs fell in the 6–8 nm range (Table 3). The considerably higher LFD value for cladophora explains why its A_{water} (Fig. 2) value was so much lower (Table 5).

Conclusions

Sulfated CNCs prepared from various materials and HCl produced pulp-CNCs were investigated for differences in the supramolecular structures. In addition to crystallinity, CNCs accessibility to water, CH_2OH conformations ratio, and chain conformational disorder were measured to define the overall supramolecular structure. The chain conformational disorder method was developed in the present work and is based on the intensity of the 900 cm^{-1} band in the Raman spectra. Compared to the structures of the CNCs from cotton MCC, bacterial cellulose, tunicin, and cladophora, the supramolecular structures of poplar and kraft pulp CNCs were found to be significantly different. In general, the structures of the CNCs were representative of the starting materials and, therefore, upon production of the CNCs their supramolecular structures were not significantly altered by the sulfuric acid hydrolysis. The methods used here are capable of characterizing CNCs and other cellulose materials irrespective of their means of production.

Supplementary material

Supplementary material contains Figs. S1 to S7 and description of the method used to isolate CNCs from kraft pulp using HCl.

Acknowledgments The authors thank Ms. Debby Sherman (DSimaging, LLC) for obtaining the TEMs of CNCs. Help of Dr. Tomas Larsson and Ms. Jasna Srndovic (Biorefinery & Energy, RISE Bioeconomy, Stockholm, Sweden) in obtaining MAS-NMR data and carrying out the analyses (CrIs and LFDs) is gratefully acknowledged. Ms. Jane O'Dell (FPL) assistance is recognized for help in obtaining some of the TGA data. General help provided by Dr. Robert Moon (FPL) is appreciated. The authors gratefully acknowledge use of X-ray facilities and instrumentation supported by NSF through the University of Wisconsin-Madison Materials Research Science and Engineering Center (DMR-1121288).

Author contributions The manuscript was written through contributions of all authors. All authors have given approval to the final version of the manuscript.

References

Abushammala H, Krossing I, Laborie MP (2015) Ionic liquid-mediated technology to produce cellulose nanocrystals directly from wood. Carbohydr Polym 134:609–616

Agarwal UP (2017) Raman spectroscopy in the analysis of cellulose nanomaterials, In: Agarwal UP, Atalla RH, Isogai A (eds.) Nanocelluloses: their preparation, properties, and applications, ACS symp. Series, American Chemical Society, pp 75–90

Agarwal UP, Ralph SA, Baez C, Reiner RS, Verrill SP (2017) Effect of sample moisture content on XRD-estimated cellulose crystallinity index and crystallite size. Cellulose 24:1971–1924

Agarwal UP, Ralph SA, Reiner RS, Baez C (2016) Probing crystallinity of never-dried wood cellulose with Raman spectroscopy. Cellulose 23:125–144

Agarwal UP, Ralph SA, Reiner RS, Hunt CG, Baez C, Ibach R, Hirth KC (2018a) Production of high lignin-containing and lignin-free cellulose nanocrystals from wood. Cellulose 25:5791–5805

Agarwal UP, Ralph SA, Reiner RS, Baez C (2018) New cellulose crystallinity estimation method that differentiates between organized and crystalline phases. Carbohydr Polym 190:260–270

Agarwal UP, Reiner RS, Ralph SA (2010) Cellulose I crystallinity determination using FT–Raman spectroscopy: univariate and multivariate methods. Cellulose 17:721–733

Agarwal UP, Reiner RS, Ralph SA (2013) Estimation of cellulose crystallinity of lignocelluloses using near-IR FT–Raman spectroscopy and comparison of the Raman and Segal-WAXS methods. J Agric Food Chem 61:103–113

Angle´s MN, Dufresne A (2000) Plasticized starch/tunicin whiskers nanocomposites. 1. Structural analysis. Macromolecules 33:8344–8353

Araki J, Wada M, Kuga S, Okano T (1999) Influence of surface charge on viscosity behavior of cellulose microcrystal suspension. J Wood Sci 45:258–261

Atalla RH, Vanderhart DL (1984) Native cellulose: a composite of two distinct crystalline forms. Science 223:283–285

Aulin C, Ahola S, Josefsson P, Nishino T, Hirose Y, Österberg M, Wågberg L (2009) Nanoscale cellulose films with different crystallinities and mesostructures—their surface properties and interaction with water. Langmuir 25:7675–7685

Azizi MASA, Alloin F, Paillet M, Dufresne A (2004) Tangling effect in fibrillated cellulose reinforced nanocomposites. Macromolecules 37:4313–4316

Bian H, Chen L, Dai H, Zhu JY (2017) Integrated production of lignin containing cellulose nanocrystals (LCNC) and nanofibrils (LCNF) using an easily recyclable di-carboxylic acid. Carbohydr Polym 167:167–176

Bondeson D, Mathew AP, Oksman K (2006) Optimization of the isolation of nanocrystals from microcrystalline cellulose by acid hydrolysis. Cellulose 13:171–180

Brinkmann A, Chen M, Couillard M, Jakubek ZJ, Leng T, Johnston LJ (2015) Correlating cellulose nanocrystal particle size and surface area. Langmuir 32:6105–6114

Chen L, Wang Q, Hirth K, Baez C, Agarwal UP, Zhu JY (2015) Tailoring the yield and characteristics of wood cellulose nanocrystals (CNC) using concentrated acid hydrolysis. Cellulose 22:1753–1762

Chen L, Zhu JY, Baez C, Kitin P, Elder T (2016) Highly thermal-stable and functional cellulose nanocrystals and nanofibrils produced using fully recyclable organic acids. Green Chem 18:3835–3843

Chi K, Catchmark JM (2017) The influences of added polysaccharides on the properties of bacterial crystalline nanocellulose. Nanoscale 9:15144–15158

Dahlke B, Larbig H, Scherzer HD, Poltrock R (1998) Natural fiber reinforced foams based on renewable resources for automotive interior applications. J Cell Plastics 34:361–379

Domingues R, Gomes ME, Reis RL (2014) The potential of cellulose nanocrystals in tissue engineering strategies. Biomacromol 15:2327–2346

Dunlop MJ, Acharya B, Bissessur R (2020) Study of plant and tunicate based nanocrystalline cellulose in hybrid polymeric nanocomposites. Cellulose 27:249–261

Elazzouzi-Hafraoui S, Nishiyama Y, Putaux J-L, Heux L, Dubreuil F, Rochas C (2008) The shape and size distribution of crystalline nanoparticles prepared by acid hydrolysis of native cellulose. Biomacromol 9:57–65

Fang L, Catchmark JM (2014) Structure characterization of native cellulose during dehydration and rehydration. Cellulose 21:3951–3963

Foster EJ, Moon RJ, Agarwal UP, Bortner MJ, Bras J, Camarero-Espinosa S, Chan KJ, Clift MJD, Cranston ED, Eichhorn SJ, Fox DM, Hamad WY, Heux L, Jean B, Korey M, Nieh W, Ong KJ, Reid MS, Renneckar S, Roberts R, Shatkin JA, Simonsen J, Stinson-Bagby K, Wanasekara N, Youngblood J (2018) Current characterization methods for cellulose nanomaterials. Chem Soc Rev 47:2609–2679

Frost B, Foster EJ (2019) Replication of annulus fibrosus through fabrication and characterization of polyurethane and cellulose nanocrystal composite scaffolds. Nanocomposites 5:13–27

Guo J, Catchmark JM (2012) Surface area and porosity of acid hydrolyzed cellulose nanowhiskers and cellulose produced by *Gluconacetobacter xylinus*. Carbohydr Polym 87:1026–1037

Goetz L, Mathew A, Oksman K, Gatenholm P, Ragauskas AJ (2009) A novel nanocomposite film prepared from cross-linked cellulosic whiskers. Carbohydr Polym 75:85–89

Grunert M, Winter WT (2002) Nanocomposites of cellulose acetate butyrate reinforced with cellulose nanocrystals. J Polym Environ 10:27–30

Habibi Y (2014) Key advances in the chemical modification of nanocelluloses. Chem Soc Rev 43:1519–1542

Habibi Y, Lucia LA, Rojas OJ (2010) Cellulose nanocrystals: chemistry, self-assembly, and applications. Chem Rev 110:3479–3500

Helbert W, Cavaille JY, Dufresne A (1996) Thermoplastic nanocomposites filled with wheat straw cellulose whiskers. Part I: processing and mechanical behavior. Polym Compos 17:604–611

Hirai A, Inui O, Horii F, Tsuji M (2009) Phase separation behavior in aqueous suspensions of bacterial cellulose nanocrystals prepared by sulfuric acid treatment. Langmuir 25:497–502

Heux L, Chauve G, Bonini C (2000) Nonflocculating and chiral nematic self-ordering of cellulose microcrystals suspensions in nonpolar solvents. Langmuir 16:8210–8212

Horikawa Y, Shimizu M, Saito T, Isogai A, Imai T, Sugiyama J (2018) Influence of drying of chara cellulose on length/length distribution of microfibrils after acid hydrolysis. Int J Biol Macromol 109:569–575

Horii F, Hirai A, Kitamaru R (1983) Solid-state 13C-MAS-NMR study of conformations of oligosaccharides and cellulose—conformation of CH2OH group about the exocyclic C–C bond. Polym Bull 10:357–361

Howsmon JA, Marchessault RH (1959) The ball-milling of cellulose fibers and recrystallization effects. J Appl Polym Sci I:313–322

Hult E-L, Larsson PT, Iversen T (2000) A comparative CP/MAS ^{13}C-MAS-NMR study of cellulose structure in spruce wood and kraft pulp. Cellulose 7:35–55

Hult E-L, Larsson PT, Iversen T (2001) Cellulose fibril aggregation—an inherent property of kraft pulps. Polymer 42:3309–3314

Jiang F, Hsich Y-L (2017) Rice straw nanocelluloses: process-linked structures, properties, and self-assembling into ultra-fine fibers. In: Agarwal UP, Atalla RH, Isogai A (eds) Nanocelluloses: their preparation, properties, and applications, ACS Symp. Series, American Chemical Society, pp 133–150

Jorfi M, Roberts MN, Foster EJ, Weder C (2013) Physiologically responsive, mechanically adaptive bio-nanocomposites for biomedical applications. ACS Appl Mater Interfaces 5:1517–1526

Klemm D, Kramer F, Moritz S, Lindstrom T, Ankerfors M, Gray D, Dorris A (2011) Nanocelluloses: a new family of nature-based materials. Angew Chem Int Ed 50:5438–5466

Kose O, Tran A, Lewis L, Hamad WY, MacLachlan MJ (2019) Unwinding a spiral of cellulose nanocrystals for stimuli-responsive stretchable optics. Nat Commun 10:510

Kvien I, Tanem BS, Oksman K (2005) Characterization of cellulose whiskers and their nanocomposites by atomic force and electron microscopy. Biomacromolecules 6:3160–3165

Larsson PT, Wickholm K, Iversen T (1997) A CP/MAS ^{13}C MAS-NMR investigation of molecular ordering in celluloses. Carbohydr Res 302:19–25

Lemke CH, Dong RY, Michal CA, Hamad WY (2012) New insights into nano-crystalline cellulose structure and morphology based on solid-state MAS-NMR. Cellulose 19:1619–1629

Lin N, Dufresne A (2014) Surface chemistry, morphological analysis and properties of cellulose nanocrystals with gradiented sulfation degrees. Nanoscale 6:5384–5393

Lindner B, Petridis L, Langan P, Smith JC (2014) Determination of cellulose crystallinity from powder diffraction diagrams. Biopolymers 103:67–73

Ling Z, Wang T, Makarem M, Santiago Cintro´n M et al (2019) Effects of ball milling on the structure of cotton cellulose. Cellulose 26:305–328

Lu Y, Weng L, Cao X (2006) Morphological thermal and mechanical properties of ramie crystallites-reinforced plasticized starch biocomposites. Carbohydr Polym 63:198–204

Mao J, Abushammala H, Brown N, Laborie MP (2017) Comparative Assessment of Methods for Producing Cellulose I Nanocrystals from Cellulosic Sources. In: Agarwal UP, Atalla RH, Isogai A (eds) Nanocelluloses: their preparation, properties, and applications, ACS symp. Series, American Chemical Society, pp 19–53

Mokhena TC, John MJ (2020) Cellulose nanomaterials: new generation materials for solving global issues. Cellulose 27:1149–1194

Moon RJ, Martini A, Nairn J, Simonsen J, Youngblood J (2011) Cellulose nanomaterials review: structure, properties and nanocomposites. Chem Soc Rev 40:3941–3994

Nanko H, Button A, Hillman D (2005) The World of Market Pulp, WOMP LLC, Appleton WI

Natterodt JC, Sapkota J, Foster JE, Weder C (2017) Polymer nanocomposites with cellulose nanocrystals featuring adaptive surface groups. Biomacromolecules 18:517–525

Nishiyama Y, Langan P, Chanzy H (2002) Crystal structure and hydrogen-bonding system in cellulose Iβ from synchrotron X-ray and neutron fiber diffraction. J Am Chem Soc 124:9074–9082

Park S, Baker JO, Himmel ME, Parilla PA, Johnson DK (2010) Cellulose crystallinity index: measurement techniques and their impact on interpreting cellulase performance. Biotechnol Biofuels 3:10

Poaty B, Vardanyan V, Wilczak L, Chauve G, Riedl B (2014) Modification of cellulose nanocrystals as reinforcement derivatives for wood coatings. Prog Org Coat 77:813–820

Program, ImageJ, https://imagej.nih.gov/ij/

Reiner RS, Rudie AW (2013) production and applications of cellulose material. In: Postek MT, Moon RJ, Rudie AJ, Bilodeau MA (eds), TAPPI Press, Atlanta, pp 21–24

Sabo RC, Yermakov A, Law CT, Elhajjar R (2016) Nanocellulose-enabled electronics, energy harvesting devices, smart materials and sensors: A review. J Renew Mater 4:297–312

Sacui IA, Nieuwendaal RC, Burnett DJ, Stranick SJ, Jorfi M, Weder C, Foster EJ, Olsson RT, Gilman JW (2014) Comparison of the properties of cellulose nanocrystals and cellulose nanofibrils isolated from bacteria, tunicate, and wood processed using acid, enzymatic, mechanical, and oxidative methods. ACS Appl Mater Interfaces 6:6127–6138

Smyth M, Rader C, Bras J, Foster EJ (2018) Characterization and mechanical properties of ultraviolet stimuli-responsive functionalized cellulose nanocrystal alginate composites. J Appl Polym Sci 135:45857

Vanderfleet OM, Reid MS, Bras J, Heux L, Godoy-Vargas J, Panga MKR, Cranston ED (2019) Insight into thermal stability of cellulose nanocrystals from new hydrolysis methods with acid blends. Cellulose 26:507–528

Wada M, Okano T, Sugiyama J (1997) Synchrotron-radiated X-ray and neutron diffraction study of native. Cellulose 4:221–232

Wang N, Ding E, Cheng R (2007) Thermal degradation behaviors of spherical cellulose nanocrystals with sulfate groups. Polymer 48:3486–3493

Wickholm K, Larsson PT, Iversen T (1998) Assignment of noncrystalline forms in cellulose I by CP/MAS ^{13}C MAS-NMR spectroscopy. Carbohydr Res 312:123–129

Wormald P, Wickholm K, Larsson PT, Iversen T (1996) Conversions between ordered and disordered cellulose: Effects of mechanical treatment followed by cyclic wetting and drying. Cellulose 3:141–152

Yang J, Han C, Duan J, Xu F, Sun R (2013) Mechanical and viscoelastic properties of cellulose nanocrystals reinforced poly(ethylene glycol) nanocomposite hydrogels. ACS Appl Mater Interfaces 5:3199–3207

Yang H, Wang T, Oehme D, Petridis L, Hong M, Kubicki JD (2018) Structural factors affecting ^{13}C MAS-NMR chemical shifts of cellulose: a computational study. Cellulose 25:23–36

Yao W, Weng Y, Catchmark JM (2020) Improved cellulose X-ray diffraction analysis using Fourier series modeling. Cellulose 27:5563–5579

Yu H, Qin Z, Liang B, Liu N, Zhou Z, Chen L (2013) Facile extraction of thermally stable cellulose nanocrystals with a high yield of 93% through hydrochloric acid hydrolysis under hydrothermal conditions. J Mater Chem A 1:3938–3944

Zhang YP, Chodavarapu VP, Kirk AG, Andrews MP (2012) Nanocrystalline cellulose for covert optical encryption. J Nanophotonics 6:063516